Soft Matter

Accepted Manuscript

This is an *Accepted Manuscript*, which has been through the Royal Society of Chemistry peer review process and has been accepted for publication.

Accepted Manuscripts are published online shortly after acceptance, before technical editing, formatting and proof reading. Using this free service, authors can make their results available to the community, in citable form, before we publish the edited article. We will replace this *Accepted Manuscript* with the edited and formatted *Advance Article* as soon as it is available.

You can find more information about *Accepted Manuscripts* in the Information for Authors.

Please note that technical editing may introduce minor changes to the text and/or graphics, which may alter content. The journal's standard Terms & Conditions and the Ethical guidelines still apply. In no event shall the Royal Society of Chemistry be held responsible for any errors or omissions in this *Accepted Manuscript* or any consequences arising from the use of any information it contains.

ROYAL SOCIETY OF CHEMISTRY

www.rsc.org/softmatter

Cite this: DOI: 10.1039/c0xx00000x

www.rsc.org/xxxxxx

ARTICLE

Sphere to ring morphology transformation in drying nanofluid droplets in a contact-free environment

Ankur Miglani and Saptarshi Basu*

Received (in XXX, XXX) Xth XXXXXXXXX 20XX, Accepted Xth XXXXXXXXX 20XX
DOI: 10.1039/b000000x

Understanding the transients of buckling in drying colloidal suspensions is pivotal for producing new functional microstructures with tunable morphology. Here, we report first observations and elucidate the buckling instability induced morphology transition (sphere to ring structure) in an acoustically levitated heated nanosuspension droplet using dynamic energy balance. Droplet deformation featuring formation of symmetric cavities is initiated by the capillary pressure that is two to three orders of magnitude greater than acoustic radiation pressure, thus indicating that the standing pressure field has no influence on the buckling front kinetics. With increase in heat flux, the growth rate of surface cavities and their post-buckled volume increases while the buckling time period reduces, thereby altering the buckling pathway and resulting in distinct precipitate structures. However, irrespective of the heating rate, volumetric droplet deformation exhibits linear time dependence and droplet vaporization is observed to deviate from the classical D^2-law.

I Introduction

Buckling of thin-walled structures is a ubiquitous phenomenon that is crucial to plethora of natural processes and industrial applications. These range from drying of peas and corn kernels to desiccation of pollen grains to invagination controlled embryonic development (gastrulation process) in animals and in spray drying of suspensions for manufacturing pharmaceuticals, foodstuffs and functional coatings [1-6]. In homogenous spherical shells subjected to uniform pressure, buckling instability initiates at a threshold pressure causing severe structural deformation in the form of surface cavities. Formation of these surface indentations leads to a significant reduction in the enclosed volume. However, imperfections in the shell (such as spatially varying thickness, geometrical topology and material elastic properties) reduce the critical buckling pressure and time delay to buckling onset, thereby, altering the buckling mode and the post-buckling shape [7-9]. Understanding such modulated shell response (commonly termed as *imperfection sensitivity*) is pivotal to prevent catastrophic failure of monocoque engineering structures ranging from oil tanks and sub-marines to aircraft fuselage [10].

Department of Mechanical Engineering, Indian Institute of Science, Bangalore, Karnataka – 560012, India
****E-mail: sbasu@mecheng.iisc.ernet.in***

Alternatively, the complex buckling patterns observed in drying suspensions are governed by the key precursor step involving surface agglomeration (structural skin formation) and its subsequent deformation [11-13]. This involves a complex interplay of several thermo-physical processes such as surface regression, particle agglomeration and internal liquid phase circulation where the transfer of mass, momentum and energy are tightly coupled. By manipulating the timescales of these processes either by varying functional properties (droplet size, initial solute concentration, particle size and dispersibility) or through external stimuli the precipitation and buckling dynamics can be altered [14-16]. This methodology has been exploited previously at different scales ranging from drying sessile droplets to manufacturing of custom-engineered micro-capsules, lock and key colloids and shells with thickness at nanoscale [17-19].

In this study, however, we provide first insights on the buckling of nanoparticle (NP) laden droplets, drying in a contact-free environment (levitated using ultrasound). The buckling front kinetics observed here offers new insights compared to the previously reported data on drying of levitated colloidal droplets [20-23] where no surface area reduction (or buckling process) was observed following semi-solid crust formation (although solvent evaporation still proceeded through the porous shell). Through experiments and dynamic energy balance, we predict

the rate of buckling (buckling front motion) and show how this varies with the heating rate leading to distinct ring micro-structures. The analysis is restricted only to externally heated droplets. However, for comparative evaluation, experimental measurements and physical estimates are presented for droplets vaporizing through the mechanism of acoustic streaming.

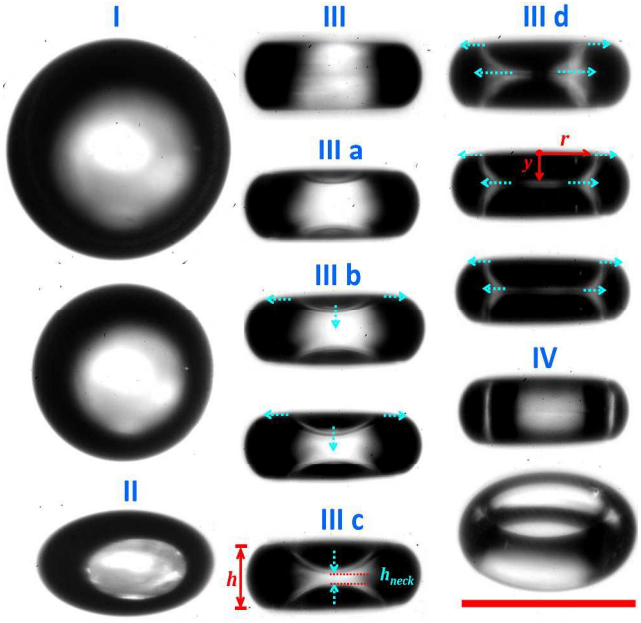

Fig. 1 Dynamic morphology transition during the vaporization and precipitation of an acoustically levitated laser irradiated nanosilica dispersion droplet at I_1 = 0.104 MW/m^2: (I) uniform volumetric shrinkage, (II) Onset of shape deformation (droplet squeezing) and subsequent transition from oblate spheroid structure to (III) disc with a toroidal edge; t_c = 0 s, (III a) Onset of buckling; Inversion of curvature with characteristic degree of deformation $h^* = \frac{h_{neck}}{h} \approx 0.85$; t_c = 0.176s, (III b) cavity growth with spreading in both radial-axial direction: formation of dimpled-disc structure ($0.08 \lesssim h^* \lesssim 0.85$); t_c = 0.276s, 0.343s and 0.51s, (III d) arrestation of buckling fronts (h^*=0) with subsequent cavity spread purely in radial direction; t_c = 0.593s, 0.77s and 0.82s (IV) merging of cavities and ring formation; t_c = 0.87s. Blue arrows indicate direction of depression growth. Scale bar equals 330 µm.

II Materials and Methods

In order to study the buckling front kinetics a single-axis ultrasonic levitator (100 kHz; 154 dB SPL) is used to suspend a 0.5±0.03 mm diameter (initial diameter D_i=2R_i) nanofluid droplet (dispersed phase: nanosilica, base fluid: de-ionized water) at the centre antinode of vertical standing wave. The droplet is irradiated with a tunable (L = 0-10W), 10.6±0.03 μm wavelength (infrared) CO_2 diode laser (beam waist diameter of 3.5 mm). Studies reported in the literature [24] have shown that with directional radiative heating, the asymmetry in temperature profile is negligible for the laser flux magnitudes used in current experiments.

The buckling instability driven morphology transition of the droplet featuring deformation of the consolidated shell is shown in Figures 1, 2 and 3. This process is captured using an ultra-high

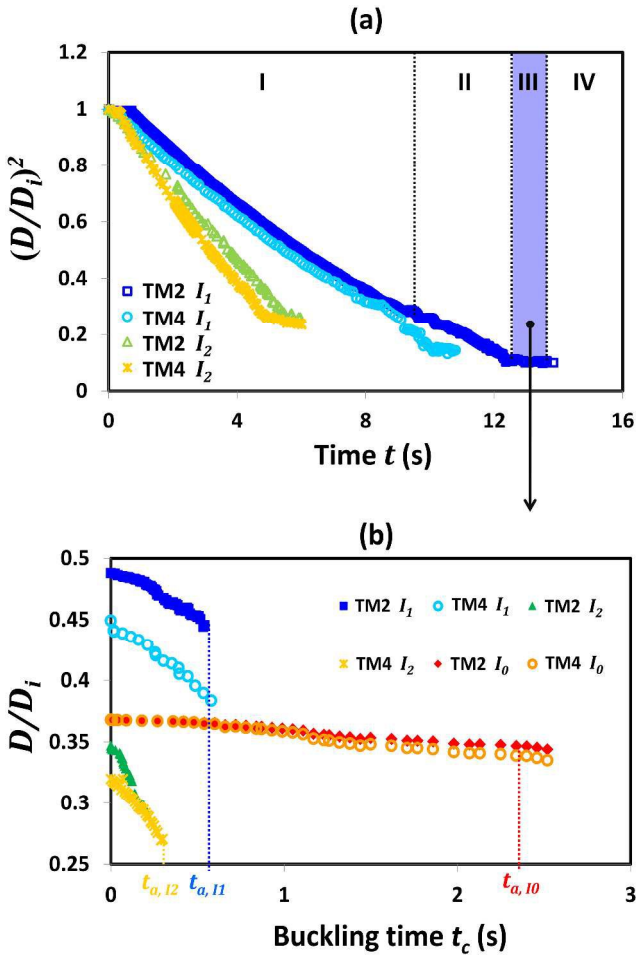

Fig. 2 (a) Time history of squared non-dimensional droplet diameter $(D/D_i)^2$ showing distinct stages of droplet lifecycle. (b) Temporal variation of droplet size reduction during the buckling regime (III).

speed monochrome Photron SA5 camera coupled with a 5X Navitar zoom lens (temporal resolution 0.33 ms; spatial resolution ~0.6 µm/pixel). The camera is synchronized with laser using an external delay generator and placed orthogonal to the laser beam axis (in the same horizontal plane). In this study, a stabilized, diluted dispersion of aqueous Ludox TM-40 nanosilica (from Sigma-Aldrich) with an average particle diameter d = 24±2nm and dispersity $Đ \sim 0.3$ is investigated at two particle loading rates c_1 = 0.764 vol. % (2 wt. %) and c_2 = 1.547 vol. % or 4 wt. % (buckling behavior is thus studied only for dilute concentrations). Henceforth these concentrations will be referred to as TM2 and TM4 respectively. In order to form a stable, long-term suspension with homogenously dispersed NPs the nanosuspension is subjected to ultrasound induced cavitation (sonication) in a constant temperature ice bath for

~30 min. Following sonication the zeta potential of colloidal suspension is measured to be
~ -50±2 mV (using zetaPALS: Phase Analysis Light scattering analyzer from Brookhaven Instruments), thus indicating a stable dispersion. These droplets are irradiated at three laser intensities:

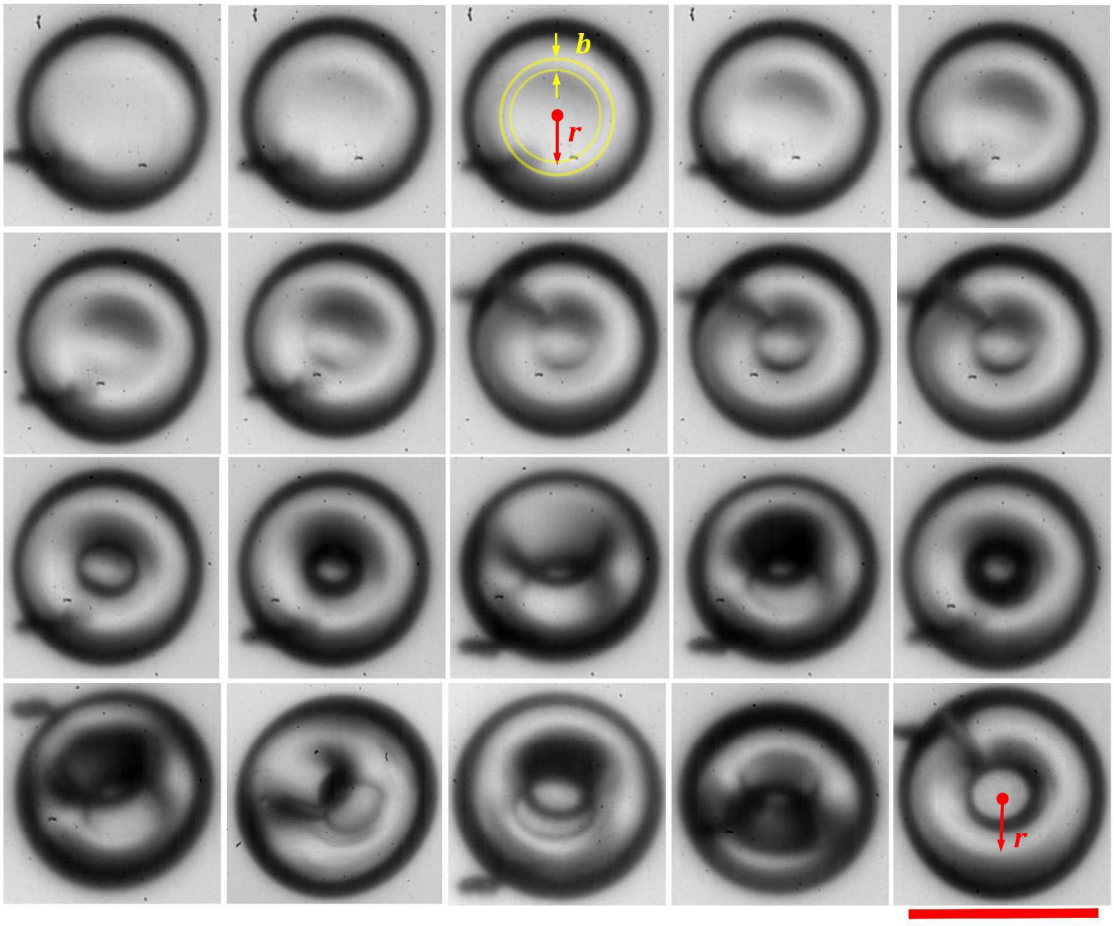

Fig. 3 High speed images showing top view of sequential cavity growth from buckling onset till doughnut-type final structure formation for acoustic streaming driven droplet vaporization (I_0 : no heating). For the image sequence the snapshots are at time instants: 0, 0.232, 0.322, 0.432, 0.616, 0.792, 0.988, 1.048, 1.188, 1.262, 1.386, 1.952, 1.956, 2.8, 2.816, 2.852, 2.908, 2.96, 3.144 and 3.296 s. Scale bar equals 220 µm.

I_0 = 0 MW/m^2 (no heating), I_1 = 0.104 MW/m^2 and I_2 = 0.208 MW/m^2. The experiments were conducted at ambient temperature (300 K) and at relative humidity RH ~ 60% (measured by TSP01 USB temperature and relative humidity probe from Thor labs).

Results and Discussion

A Dynamic Buckling Process

External heating initiates rapid solvent vaporization. The resulting solvent loss triggers a sequential three-stage droplet deformation process as shown in Figures 1 and 2: (I) isotropic droplet shrinkage for initial 65 % of the total droplet lifetime (t_I ~0.65t_e; t_e is the total evaporation time), (II) Non-uniform Bernoulli pressure (acoustic radiation pressure) governed primary deformation phase [25-27]. This features droplet flattening and gradual formation of an inhomogeneous porous shell with minimum thickness at the poles (t_{II} ~0.25t_e). Mass diffusion Peclet number for the droplet is given by $Pe_m = \frac{t_{Diffusion}}{t_e} = \frac{R_i^2/D_a}{t_e}$ and is in the range $5 < Pe_m < 250$ (D_a ~ 5.6 X 10^{-11} m^2/s is the particle diffusion coefficient obtained from Stokes-Einstein relation [28]). High value of Peclet number (Pe_m) indicates that the timescale for homogenizing the internal composition (driven by particle diffusion) is one to two orders lower compared to the rate of droplet surface regression. This causes dispersed nanoparticles to accumulate at the droplet sub-surface as the liquid-vapor interface recedes continuously, resulting in the formation of a viscoelastic shell. Inhomogeneity in the shell (spatially varying

Cite this: DOI: 10.1039/c0xx00000x
www.rsc.org/xxxxxx

ARTICLE

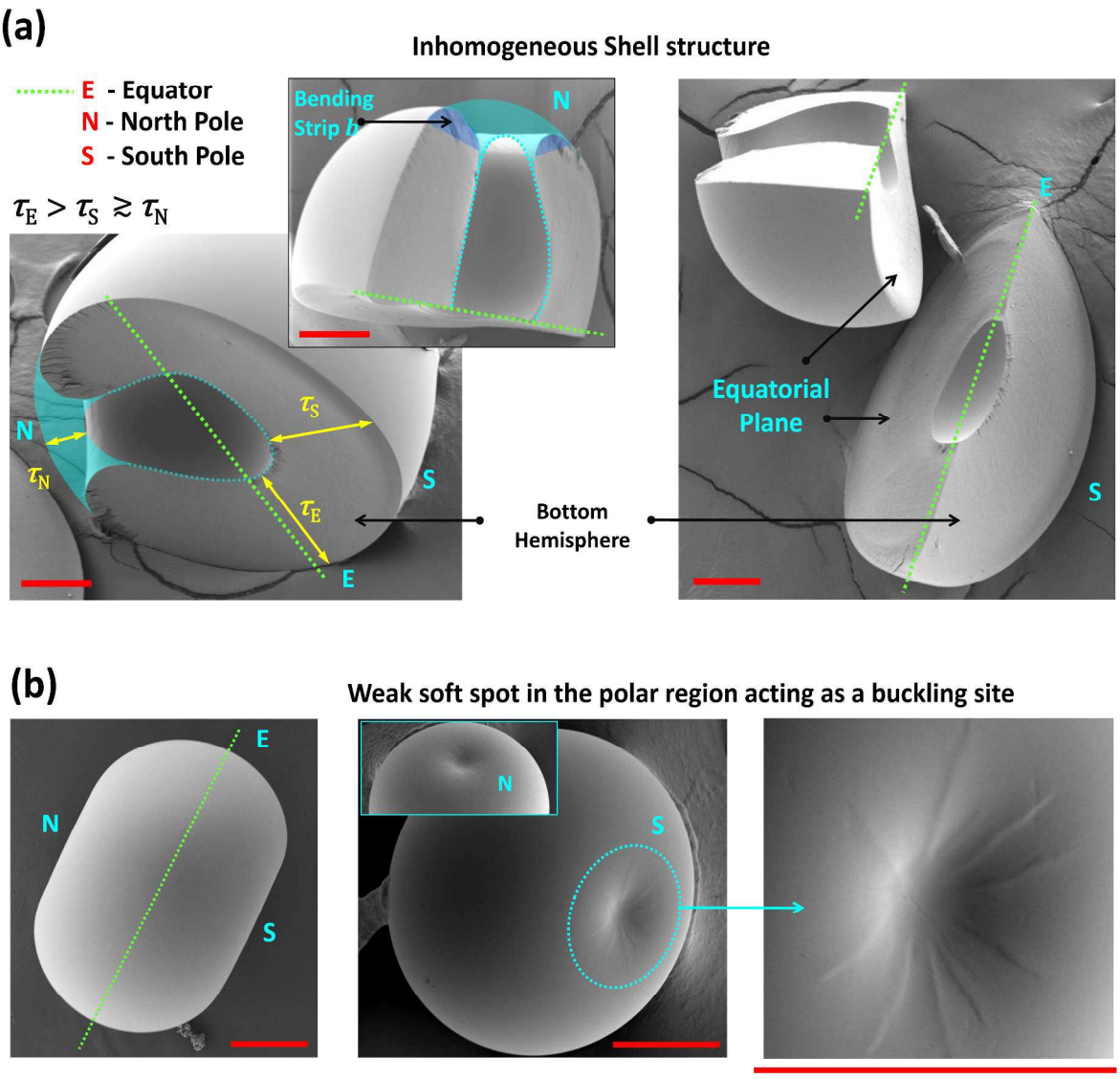

Fig. 4(a) SEM micrographs showing cut-section through the final precipitate microstructure of an acoustically levitated nanofluid droplet (with dense particle loading rate 10 Vol. %) dried at no lasing condition (I_0 = 0 MW/m^2). (b) SEM images illustrating precipitate structures obtained at near buckling onset for nanofluid droplet (TM2; c_1 = 2 wt. %) dried at no lasing condition (I_0 = 0 MW/m^2). These indicate locations of buckling sites (weak soft spots in the shell). All scale bars equal 50 μm.

thickness) is however induced at two levels: (1) $\tau_N \leq \tau_S$ i.e. average shell thickness τ_N at the top (North Pole region N) is nominally smaller than at the bottom τ_S (South Pole region S). This differential thickness is induced by the acoustic streaming driven internal flow field which becomes asymmetric as the droplet shifts from pressure node (due to the presence of gravitational field). This asymmetric recirculation (with stronger recirculation in bottom hemisphere) or orthokinetic particle transport mechanism causes preferential particle accumulation in the lower-half and forms a thickened bottom structure [29-31]. (2) $\tau_E > \tau_N, \tau_S$ i.e. equatorial region E is thicker than the poles. Shell formation with non-uniform thickness is evident from SEM micrographs (Fig. 4) for a representative case; drying nanofluid droplet at dense NP concentrations (c = 10 vol. %),

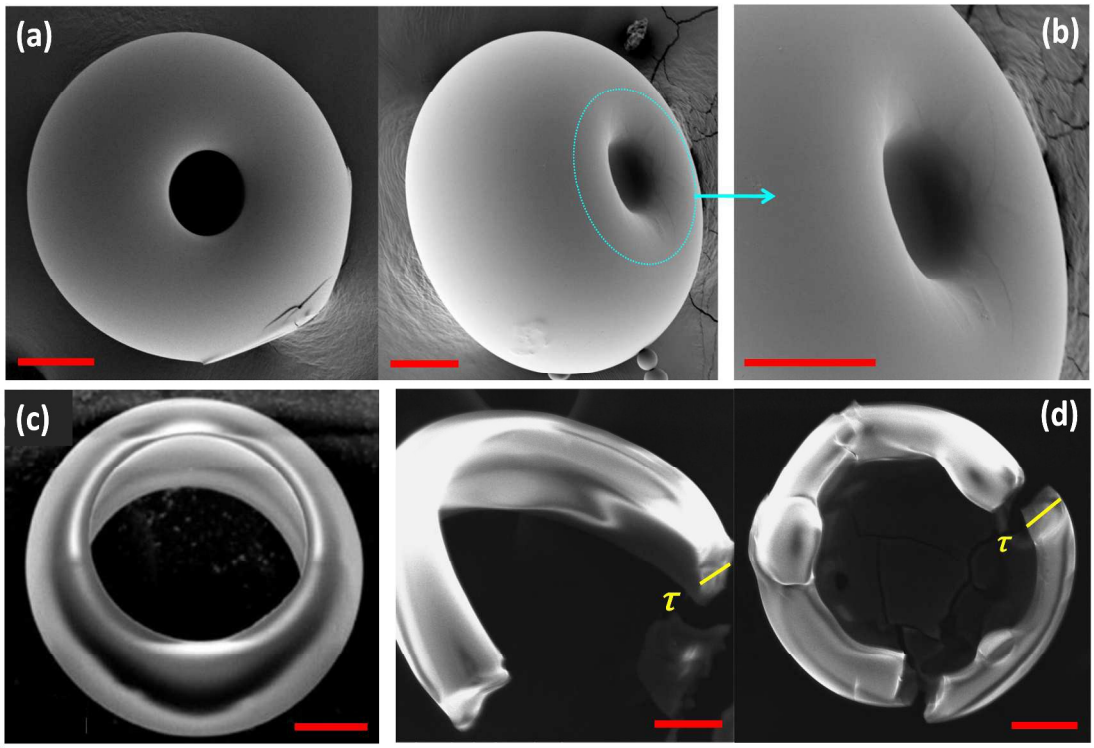

Fig. 5 SEM micrographs showing final precipitate structures at three laser intensities (a) No lasing; formation of doughnut-type microstructure, (b) magnified view of narrow bending strip region around the collapsed top sector (c) I_1 = 0.104 MW/m^2; formation of thick, smooth ring and (d) I_2 = 0.208 MW/m^2; formation of thin, corrugated rings that fracture at higher capillary pressures. All scale bars equal 50 μm.

under no lasing condition. The cut section (along meridional plane) through final precipitate clearly illustrates heavy particle deposition along the equatorial belt while the shell narrows gradually at the top (near North Pole) forming a weak circular sector that eventually buckles. Normalized average thickness τ_E/R_B is ~ 0.26 while in the bending strip region b surrounding the top collapsed region τ_N/R_B ~ 0.08 and in the bottom sector τ_S/R_B ~ 0.18 (R_B is the droplet radius at buckling onset). This indicates that the shell is ~ 30-70 % thinner near to poles compared to the equator. Note that in the SEM image of Fig. 4 (a), a classical *gastrula structure* is formed (term commonly used in embryology) with only one sided (top) buckling. Caving in of the bottom portion is suppressed since at high NP loading rates (10 Vol. %) the increased fluid viscosity dampens internal recirculation. This causes particle deposition in the bottom half through differential settling and leads to a thick, rigid bottom structure that resists buckling. However, at dilute concentrations (c < 2 Vol. %) considered in this study, both top-bottom buckling is observed (discussed subsequently) that forms a *ring*. In summary, shell thickness τ is a critical parameter that determines the stress required to initiate shell deformation and its inhomogeneity is induced such that *Polar Regions become weak soft spots and act as preferred buckling sites*. Formation of these *weak soft spots* at near buckling onset is evident in Fig. 4b.

First order estimate of the average shell thickness τ is obtained from particle mass conservation assuming that the concentration increases until a random packing fraction (vol. %) of c_f = 0.56 is achieved.

$$\tau = R_B\left[1-\left(\frac{c_f-c_i(R_i/R_B)^3}{c_f-c_i}\right)^{\frac{1}{3}}\right] \quad (1)$$

τ obtained from Eq. 1 is ~15±7 μm which is of the same order as that estimated from the SEM micrographs (~25 μm) of the final precipitates (Fig. 5).

Subsequently, in the secondary deformation phase (III) governed by meniscus or capillary forces, the thin-walled elastic shell with *Foppl-von Karman number* $\alpha \approx 10\left(\frac{R_B}{\tau}\right)^2$ ($850 \lesssim \alpha \lesssim 1150$) undergoes inversion of curvature at the poles marking buckling onset (III a). The resultant polar depressions grow and invaginate

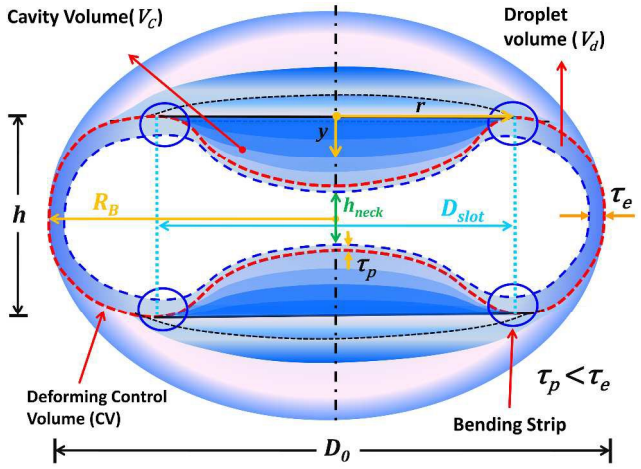

Fig. 6 Schematic showing superimposed surface profiles of a buckling nanofluid droplet; critical buckling parameters are marked.

inside the droplet (Fig. 1) exhibiting a two-sided, opposed, near-symmetric buckling (maximum difference in the time-averaged volumetric growth rate of top-bottom cavities is <10%). Particularly, the bottom depression growth is marginally slower due to its increased rigidity (as discussed previously). Time delay to buckling onset corresponds to ~93±4% reduction in the droplet volume and occurs during final 1% and 5% of the droplet lifetime at I_0 and I_1, I_2 respectively.

In particular, cavity growth during secondary deformation proceeds in three stages (shown in Fig. 1 and later in Figures 8d, 8e and 8f): (III b) In tandem radial-longitudinal expansion; in this regime, the radial spread rate of cavity ($\dot{r}$) varies with heating rate such that $\dot{r}_{I_2} \approx 2\dot{r}_{I_1} > 10\dot{r}_{I_0}$, (III c) longitudinal expansion with constant cavity-rim radius and the final stage (III d) occurs following longitudinal cavity growth arrestation by the opposing buckling front; $\frac{h_{neck}}{h} = 0$ (Fig. 1) with subsequent cavity tip flattening. This regime features cavity expansion only along radial direction, however with different spreading rates at rim plane (cavity top) and equatorial plane (cavity bottom). Radial spread rate at equatorial plane is significantly higher compared to that at the rim (~5 times at I_1 and ~2.5 times at I_2). End of stage III d corresponds to maximum shape deformation (penultimate structure) prior to merging of buckling fronts and formation of ring-slot (IV).

At this point, solvent has completely vaporized and cavity shape is *naturally stabilized* by opposing sister cavity, thereby controlling the ring-slot diameter D_{slot} of final precipitate structure (shown inset in Fig. 7). The buckling fronts finally merge to form ring microstructure ($t_{III} \sim 0.1t_e$) as shown in the SEM images (Fig. 5). Under no laser heating, however, regime III d is absent and transition from cavity tip merging to ring formation occurs in single step. Thus, occurrence of regime III substantiates that the droplet surface regression continues even after porous shell formation and the rate of surface retraction increases with heating rate (as shown in Fig. 2b). Particularly, during the buckling phase (regime III), the time-mean droplet surface regression rate (characterized by the buckling front motion) $\frac{dR}{dt}$ at I_2 is *O* (10^{-2} mm/s). This is ~3-4 times faster compared to I_1 and an order of magnitude greater than at no heating condition I_0 (where *R* is the projected area equivalent radius).

B Effect of heating rate on buckling front motion

Post buckling onset, the depression/ cavity growth rate can be predicted from a *global energy balance* applied to a deformable control volume (CV) encapsulating the droplet (Eq. 2 below). In particular, this analysis captures the temporal variation of bending deflection or motion of cavity-tip (*y*) and holds only till cavity growth arrestation (i.e. end of stage III c). Critical length scales involved in the analysis are shown in Fig. 6:

$$\dot{Q} = 2\dot{W}_{ext} + \frac{d\,(U_{int})}{dt} + 2\rho_w \left(\frac{dV_c}{dt}\right).h_g \qquad (2)$$

where, $\dot{Q} = I.\pi R_B^{*2}$ is the external heat energy input effecting droplet gasification (where, R_B^* is the projected area equivalent radius of the droplet and I is the laser intensity). Factor 2 is added in the first and last terms due to the guided, symmetric folding of top-bottom cavities. In Eq. 2, convective heat transfer resulting from acoustic streaming (which also contributes to droplet gasification) is neglected since it is negligible compared to the laser heat flux. This is indicated by significantly shorter (2-3 orders of magnitude) droplet evaporation time scale (i.e. total droplet lifetime t_e) at lasing conditions (t_e~ 6s at I_2 and t_e~ 15 s at I_1) compared to that under acoustic streaming vaporization [t_e~ *O* (1000s)].

During the *cavity growth phase* (measured as the time period t_m from buckling onset till the merging of top-bottom buckling fronts) the projected droplet aspect ratio $AR_B = D_0/h$ (and hence the available projected area for heating) remains constant and droplet exhibits no lateral contraction. Consequently, the change in structural morphology is solely due to depression growth in radial-longitudinal direction. Further, as caving in proceeds, the amount of solvent vaporized at each instant corresponds to volume displaced by the cavity. This solvent mass extracts latent heat and the resulting vaporization flux drains energy ($\rho_w \left(\frac{dV_c}{dt}\right).h_g$) from the droplet as it crosses CV (h_g is the saturated vapor enthalpy at spatially averaged droplet temperature T_{avg}). Thus, during buckling transition, micro-structure remains axisymmetric and the enclosed droplet volume reduces such that $2V_c + V_d = constant = V_{dB}$ at each instant (V_{dB} is the volume of flat, disc shaped structure with a toroidal edge that is formed at buckling onset) or

$$2\frac{dV_c}{dt} = -\frac{dV_d}{dt} \qquad (3)$$

or, Cavity growth rate = Droplet deformation rate

Cite this: DOI: 10.1039/c0xx00000x

www.rsc.org/xxxxxx

ARTICLE

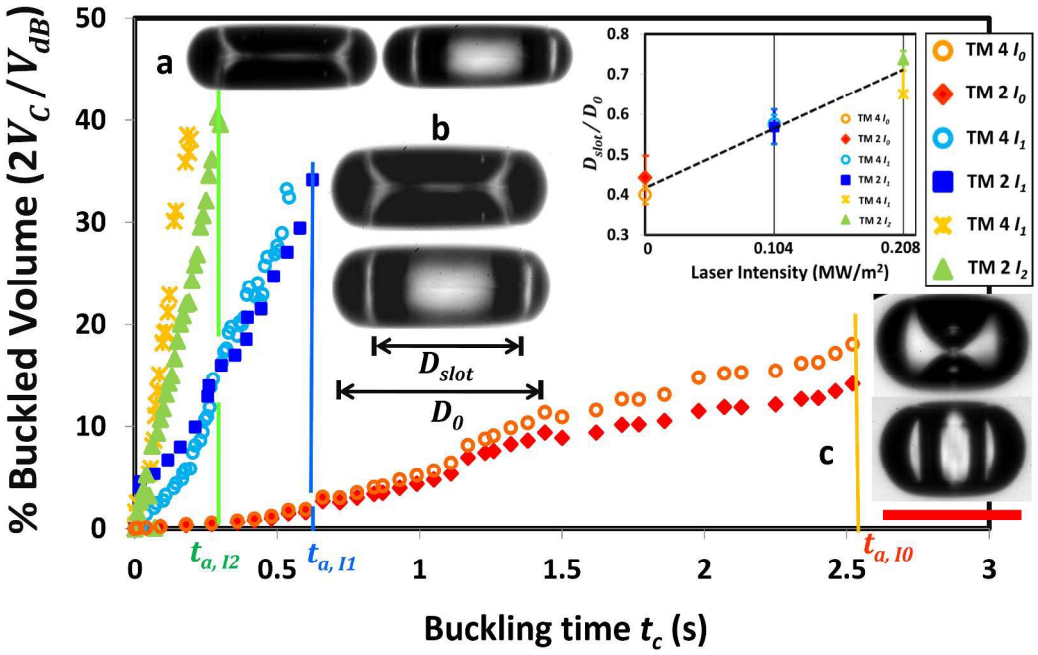

Fig. 7 Temporal variation of normalized cavity volume ($2V_C/V_{dB}$) during the secondary deformation, buckling phase. Image pairs showing rapid transformation (~1ms) from penultimate structure to ring slot formation; Inverted plateau-type cavities with high flatness ratio $f_c = \frac{r-h/2}{r}$ (a) f_c ~0.55 at I_2 and P_B ~0.7 MPa, (b) f_c ~ 0.4 at I_1 and P_B ~0.22 MPa: Both resulting in broader ring-slots and (c) elongated, paraboloid wok-type cavities with f_c ~ 0.24 at I_0 and P_B ~0.025 MPa resulting in narrow slots. Inset shows the variation of relative ring-slot diameter (D_{slot}/D_0) at these conditions. Buckling timescales (tare indicated by vertical lines and mark the point of cavity growth arrestation. Scale bar for all images equals 220μm.

The external *moving boundary work* is given by $\dot{W}_{ext} = -2(P_B + P_{a,rms}).\frac{dV_c}{dt}$, where $P_B = \frac{\mu.J.\tau}{k}$ is the capillary pressure drop (obtained from Darcy's law) that is required to percolate the solvent through porous shell and drives the shell deformation. $J = \frac{dR}{dt}$ is the solvent vaporization flux through the porous shell per unit surface area at buckling onset and measured to be of the order of 10^{-6} m/s and 10^{-5} m/s at no lasing and lasing conditions respectively. k is the shell permeability obtained from Kozeny–Carman equation $k = \frac{1}{180}\frac{(1-c_f)^3}{c_f^2}d^2$ and μ is the dynamic viscosity of continuous phase/solvent (water). It should be noted here that the solvent viscosity μ is considered in evaluating P_B since the fluid flowing through the pores would not carry any free NP's. Suspended NP's would deposit on the shell itself since the extremely small sized pores would necessarily exclude their transport across the consolidated shell. However, the droplet viscosity increases continuously due an increase in the surface concentration of solute. This can be calculated as $\mu_d = \mu\ (1+2.5c_B+6.5c_B^2)$ [32], where $c_B = c_i\ (R_i/R_B)^3$ is the volumetric particle concentration at buckling onset.

At a critical magnitude of capillary pressure (or buckling pressure) the shell undergoes a *sol-gel transition* and marks the onset of buckling. At this point the deformation inducing, attractive capillary forces between nanoparticles (NP) overcome the stabilizing electrostatic repulsive forces, thus transforming the shell from a viscous fluid to an elastic porous structure of densely packed particles [33]. Based on Darcy' Law order of magnitude of P_B is estimated to be ~ 0.03 MPa, 0.3 MPa and ~1 MPa at I_0, I_1 and I_2 laser settings respectively. Thus, with an increase in external heating rate the capillary pressure increases. At buckling onset P_B corresponds to the external critical buckling pressure given by the linear buckling shell theory i.e. $P_{cr}^* \sim 10\frac{Y}{\alpha}$ (where Y is the shell's Young's modulus). P_{cr}^* is the threshold corresponding to the maxima of the shell's total free energy beyond which the cavity is in a unstable equilibrium state and grows spontaneously on its own accord, when $y \sim \tau$ [34]. Indeed, our experimental measurements show that the inversion depth y (corresponding to the line of maximum cavity deformation) is ~ 7±1.5 μm at I_0, 9±2 μm at I_1 and 8±2 μm at I_2 which is of same order of magnitude as shell thickness τ

(~15±7 μm) predicted from Eq. 1. Given that cavity radius r << R_B and based on the condition that inversion depth $y \sim Y^2.\tau^5/R_B^4.P_B^2$ is of same the order as τ when the external pressure P_B equals the buckling pressure $P_{cr}{}^*$, Young's Modulus Y is predicted to be in the range ~O (0.002-2) GPa. It will be shown later that even with a three orders of magnitude variation in Y the prediction of cavity growth rate remains unaltered.

Next, the RMS acoustic sound pressure of standing wave is significantly smaller $P_{a,rms}$ = 0.02 ($10^{SPL/20}$) ~ 1 KPa [35]. P_B >> $P_{a,\,rms}$ is indicative that P_B is the principle pressure force that triggers buckling instability while the surrounding ultrasonic pressure field only plays a supporting role in pre-buckling stages. Particularly, the acoustic field is responsible for the droplet flattening and inducing in-homogeneity in the shell. Shell deformation due to capillary forces arises principally due the formation of several menisci with large interfacial curvatures (in the gaps between particles). The resultant pulling tensile forces generated due to menisci curvature pushes the particles inwards and pulls solvent to the outer periphery [33]. As such, buckling of porous particle shell initiated by capillary pressure appears to be a universal phenomenon in drying colloidal droplets. This is primarily governed by the shell formation process and exhibits rather weak dependence on the environment since it has been previously observed in drying sessile droplets on hydrophobic substrate [3], levitated Leidenfrost droplets [33] and in droplets sandwiched between circular glass slides [36].

Note that since P_B is a direct measure of the *severity of buckling* and Pe_m controls the shell formation process, the synergistic effect of these parameters determines the rate of cavity growth and post-buckling reduction in droplet volume. In other words, these parameters govern the *buckling pathway* and the *post-buckling* final structure of the precipitate. This is indicated by a faster rate of increase of the relative cavity volume ($2V_c/V_{d,B}$) with P_B and inverse dependence of buckling timescale (t_c) on P_B and Pe_m. These features are shown in Fig. 7 and indicate that higher heating rates result in thinner rings that tend to fracture due to higher P_B (as shown in Fig. 5 SEM images). The buckling timescale t_c at high laser flux I_2 (~0.2s) is ~ three times lower compared to that at I_1 (0.6 s) and an order lower than the no heating case (~3 s). Also, experimentally measured time-mean growth rate of cavity-tip is $(\dot{y})_{I_0} \approx$ 0.02±0.002 mm/s, $(\dot{y})_{I_1} \approx$0.11±0.018 mm/s and $(\dot{y})_{I_2} \approx$ 0.22±0.02 mm/s). Since cavity tip lies along the line of maximum deformation and $2\dot{y} = -\dot{h}_{neck}$ (marked in Fig. 1), the magnitudes of $\dot{y}$ indicate that the *rate of droplet necking* doubles with laser intensity while it is an order lower under pure vaporization. Similarly, the corresponding time-averaged, volume collapse rate ($\dot{V}_d$) at lasing conditions (O (10^{-3} mm^3/s)) is an order higher than at I_0. Also, the fraction of collapsed droplet volume at the point of arrestation (t_a) is ~twice than under pure gasification. However, at the penultimate stage the percentage of buckled droplet volume at high laser flux condition (I_2) is ~ 3 times compared to that at I_0.

Next, the shell internal energy contribution comes from two components:

$$U_{int} = m_d c_v T_{avg} + 2E \tag{4}$$

where, $m_d(t) = \rho_d V_d$ is the time varying droplet mass and ρ_d is droplet density. E is the part of internal energy associated with the morphology adopted by the shell. Particularly, it is the total elastic energy stored in the buckled shell that varies dynamically as depth of the bulge increases continuously and droplet attains different geometric variants of a *dimpled-disc structure*. It comprises of four components:

$$E = E_0 + E_{BS} + E_I + E_{SS} \tag{5}$$

where, E_0 is the constant reference energy of the shell in undeformed state, $E_{BS} = E_B + E_S \approx 4\pi rb.Y.\left(\frac{\tau^2}{R_B{}^2}\right).y$ is the total elastic energy stored in the narrow stress concentration rim (bending strip) of width b and is linear in indentation depth or bending deflection (y). This width $b \equiv \frac{R_B}{\alpha^{1/4}}$ ~32±10 µm (shown in Fig. 3) physically represents an elastic length scale over which the deformations are localized and is obtained by minimization of E_{BS} (state corresponding to equivalence of bending and stretching energies: E_B = E_S). Here, $E_B \sim 2\pi r.Y.\epsilon^2.\left(\frac{\tau}{\alpha^{1/4}}\right).y$ and $E_s \sim 2\pi r.Y.\left(\frac{\tau}{\alpha^{3/4}}\right).y$ represent the energy contributions due to bending (out-of-plane) along the longitudinal direction and stretching (in-plane) along circumferential directions respectively. During the inversion of curvature, the relative extension $\epsilon = \frac{2\theta R_B - 2\theta\,(R_B - \tau)}{2\theta R_B} = \frac{\tau}{R_B}$ resulting from the compression of the outer layers and stretching of the inner layers contributes to the elastic energy that is concentrated in the inverted cap (bulge) region $E_I \sim Y(\epsilon^2).\tau R_B y$ [34]. The last energy term $E_{SS} \approx \frac{\pi}{16}.Y.\epsilon.y^3$ represents a contribution from in-plane stretching (tensile stresses) that is generated along the cavity surface due to cavity growth in the axial direction and represents the energetically favored buckling mode as the energy E_{BS} localized in the bending strip becomes enormous. This buckling pathway features preferential cavity growth in the longitudinal direction while the lateral width ($2r$) remains constant [37]. During cavity growth period $r > b$ (this is clearly seen in Fig. 3; $r \gtrsim 2.5b$) this condition implies that $\frac{E_{BS}}{E_I} \approx \frac{r}{b} > 1$ and $\frac{E_{SS}}{E_I} \approx \left(\frac{r}{b}\right)^4 >> 1$, thus, E_I has negligible contribution in the total shell elastic energy. Internal energy change is then given by:

$$\frac{d(U_{int})}{dt} = m_d c_v \frac{dT_{avg}}{dt} + c_v T_{avg} \frac{dm_d}{dt} + 2\left(\frac{dE_{BS}}{dt} + \frac{dE_{SS}}{dt}\right) \tag{6}$$

It is noteworthy to mention here that buckling, as an instability, corresponds precisely to the lack of local energy balance

between the pressure work $P_B.\Delta V_C$ and the shell elastic energy E. The

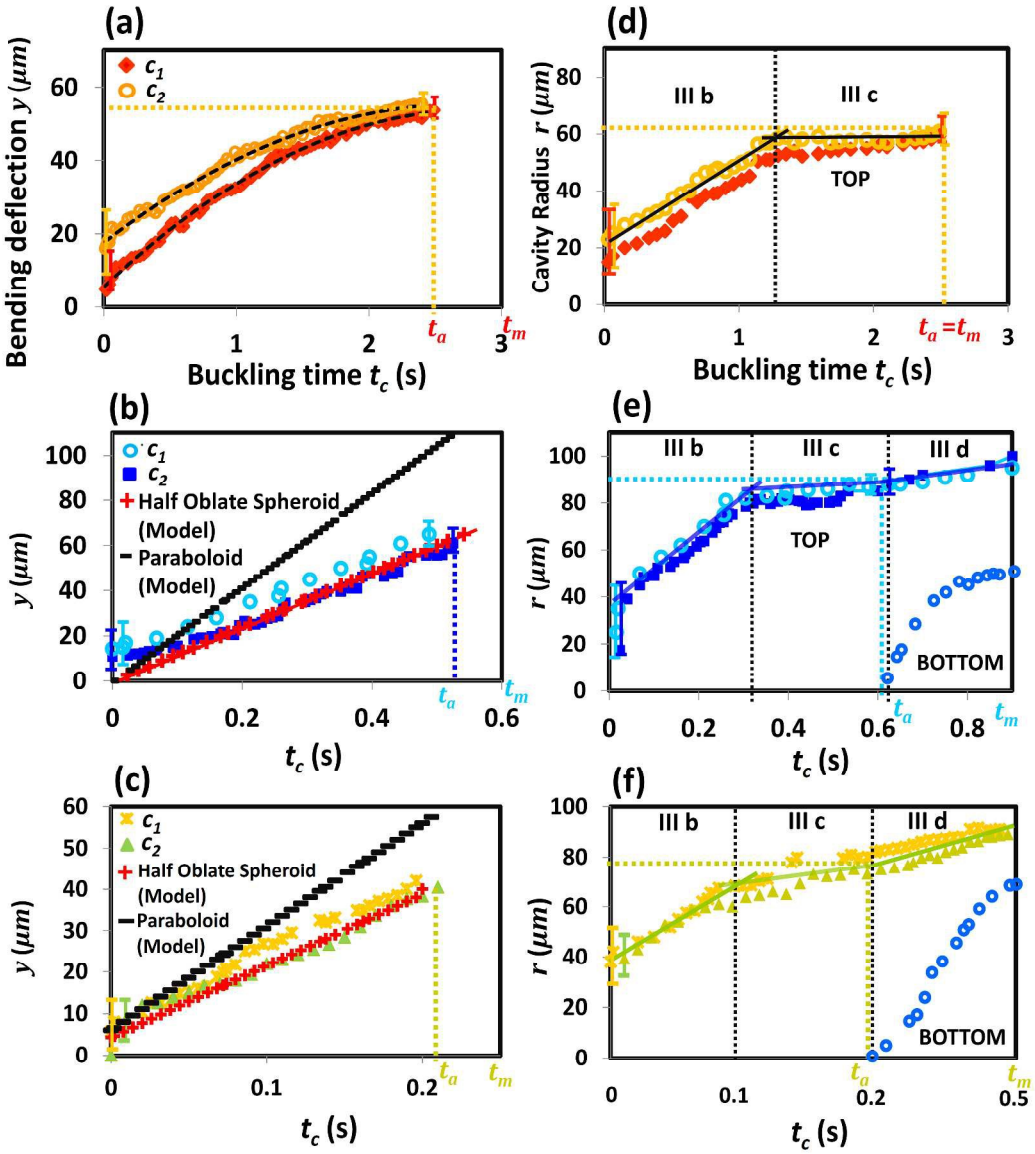

Fig. 8 Temporal variation of cavity-tip displacement (y) characterizing cavity growth in axial direction at **(a)** I_0 = 0 MW/m^2 (no heating), **(b)** I_1 = 0.104 MW/m^2 and **(c)** I_2 = 0.208 MW/m^2. Three-part, sequential growth of cavity in radial direction at the rim (Cavity TOP) and at equatorial plane (cavity BOTTOM) following cavity growth arrest (t_c=t_a) along vertical axis, at **(d)** I_0 = 0 MW/m^2 (no heating), **(e)** I_1 = 0.104 MW/m^2 and **(f)** I_2 = 0.208 MW/m^2.

energy reduction in $P_B.\Delta V_C$ dominates the energy cost of E and as a result it is energetically favorable for the shell to collapse catastrophically and reduce its internal volume. Due to the short time scale of cavity growth process (< 1s), increase in spatially averaged droplet temperature T_{avg} is nominally small (< 5°C) and T_{avg} at laser flux conditions I_1 and I_2 is ~ 40°C and ~52°C respectively. Consequently, the sensible temperature rise has negligible contribution to the internal energy change compared to the reduction resulting from mass transfer across CV i.e. $m_d c_v \frac{dT_{avg}}{dt} << c_v T_{avg} \frac{dm_d}{dt}$ and the corresponding variation in thermo-physical parameters (ρ_w = 990±5 Kg/m^3, c_v = 4.182 KJ/kg-K and h_g = 2580 KJ/Kg) due to temperature change is less than 2%. In addition, although the increase in cavity radius occurs in three steps till final ring-slot radii (discussed in previous section and shown in Fig. 8), as a first approximation we assume a time-averaged cavity radius $r^* = \frac{\int_0^{t_a} r dt}{t_a}$ till buckling front arrestation and model the cavity shape with two potential surfaces of revolution of volume $V_C = Kr^{*2}y$, (1) a paraboloid with K=1.57 and (2) half-Oblate spheroid (K=2.1). The time derivative of internal energy given by Eq. 6 reduces to:

$$\frac{d(U_{int})}{dt} = -\rho_d c_v T_{avg}.(2Kr^{*2})\frac{dy}{dt} + 2(c_0.4\pi rb.Y.\epsilon^2.\frac{dy}{dt} + c_2.\frac{3\pi}{16}.Y.\epsilon.y^2.\frac{dy}{dt}) \quad (7)$$

As solvent vaporizes, the coupled mass loss causes a continuous change in the droplet density. Thus, ρ_d in Eq. 7 is assumed as time-averaged density $\rho_d = (\int_0^{t_a} \rho dt)/t_a$ (ρ_d =1300±10 Kg/m^3 and 1340±20 Kg/m^3 at I_1 and I_2 respectively). Under laser irradiation, maximum change in shell elastic energy components given by $\frac{dE_{BS}}{dt}$ and $\frac{dE_{SS}}{dt}$ is *O* (10^{-7}) J/s and *O* (10^{-7}) J/s respectively at I_1 while the corresponding values at I_2 are *O* (10^{-6}) J/s and *O* (10^{-6}) J/s respectively. In contrast, the decrease in internal energy content due to droplet mass reduction $-\rho_d c_v T_{avg}.(2Kr^{*2})\frac{dy}{dt}$ is significantly larger *O* (10^{-2}) J/s. Therefore, net internal energy change is given by $\frac{d(U_{int})}{dt} \approx -\rho_d c_v T_{avg}.(2Kr^{*2})\frac{dy}{dt}$.

Similarly, as solvent percolates and undergoes phase change, the rate of energy transfer across CV associated with solvent mass loss and thermal energy transported along with the vapor is four orders higher *O* (10^{-2}) J/s. The rate at which displacement work is expended in deforming droplet $-P_C\frac{dV_d}{dt}$ is *O* (10^{-7}) J/s and *O* (10^{-6}) J/s respectively at I_1 and I_2. Under pure vaporization, the deformation rate work is ~3-4 orders lower (i.e. 10^{-10} J/s). These values are of the same order as the change in total shell elastic energy at their respective laser heat flux conditions. Therefore, external work term is also negligible compared to the rate of change of internal energy $\frac{d(U_{int})}{dt}$ ~*O* (10^{-2}) J/s. As such, as the droplet morphs to different deformed shapes the contribution to overall energy budget either through work done by the capillary forces or by dynamically stored shell elastic energy can be neglected. The buckling front kinetics is rather governed by energy and mass transfer effected by solvent vaporization. Since, droplet deformation rate is a direct function of the rate of increase of shell's elastic deformation energy, these first order estimates show that with an increase in heating rate the buckling front motion (or cavity spread rate) is accelerated. Based on these energy considerations, volumetric cavity growth is predicted from final energy balance as:

$$2\frac{dV_c}{dt} = \frac{I.\pi R_B^{*2}}{(-\rho_d c_v T_{avg} + \rho_w h_g)} \quad (8)$$

where, R.H.S. is constant and L.H.S. is given by $2\frac{dV_c}{dt} = -\frac{dV_d}{dt}$ = *Rate of volumetric droplet shrinkage* (from Eq. 3). Therefore, $-\frac{dV_d}{dt}$ = *Constant*. Since droplet volume at any instant during the buckling process is V_d = (π/6). D^3 (where *D* is the volume equivalent droplet diameter) and given the initial condition that $D = D_B^*$ (i.e. droplet diameter at buckling onset) at time t_c = 0, then Eq. 8 can be written as:

$$D^3(t) = D_B^{*3} - Ct_c \quad (9)$$

Eq's. 8 and 9 have following implications: First, during the cavity growth phase, droplet surface regression deviates from the linear D^2-law as volume-equivalent droplet diameter $D(t)$ exhibits $t_C^{1/3}$ dependence. Secondly, irrespective of the model assumed for cavity shape, volumetric droplet deformation rate $-\frac{dV_d}{dt}$ is constant. This is only a function of the pre-buckling aspect ratio, heating rate and thermophysical properties.

With transitional squeezing of the droplet (due to compressive acoustic radiation pressure at poles) till a constant aspect ratio (at end of primary deformation phase), the cavity growth is subsequently subjected to a geometric constraint: $y = \frac{h}{2}$ (maximum bending deflection) at $t = t_m$. This constraint implicitly considers the assistive role played by acoustic field in controlling the droplet aspect ratio at buckling onset (AR_B) and hence the maximum cavity growth possible. The buckling front motion characterized by the displacement of cavity-tip is then captured by Eq. 10 below and is illustrated in Fig. 8

$$\dot{y} = \frac{0.5(I.\pi R_B^{*2})}{kr^{*2}(-\rho_d c_v T_{avg} + \rho_w h_g)} \quad (10)$$

Eq. 10 indicates that: (1) the bending deflection (y) increases linearly with time (i.e. constant tip velocity) as the buckling front's move under a dynamic imbalance between capillary force and the resilient elastic shell deformation (while solvent percolates and gasifies) and (2) at high vaporization mass flux (I_1 and I_2) the deformed surface preferentially adopts a half-oblate spheroid

Drying nanoparticle laden droplets suspended in a container less environment (acoustically levitated) undergo morphology transition from an initial sphere to a final ring-shaped precipitate structure. This transition is induced by the capillary pressure initiated buckling of a porous elastic crust; which forms through the consolidation of NPs (as the droplet vaporizes). Based on a global energy balance of the droplet (involving an order of magnitude comparison of different energy terms), we conclude that during the buckling process droplet gasification deviates from the classical D^2-law. Particularly, the rate of droplet deformation or the volumetric growth of surface

geometry compared to a paraboloid. These features are illustrated in Figures 8b and 8c and indicate that assuming paraboloid geometry, the cavity tip growth is significantly over predicted (Note that spherical cap geometry has not been considered to model the cavity since its volume lies mid-way between the assumed curves). In contrast, the experimental data at no lasing condition shows that the cavity tip growth is rather quadratic in time (Fig. 8a).

IV Conclusion

cavities is linear in time and hence exhibits linear variation of D^3 *vs.* time. Besides, by increasing the input laser flux, both the shell buckling rate (cavity front motion) and the degree of droplet deformation can be enhanced thereby leading to distinct microstructures. Such controlled manipulation of the buckling front kinetics can be exploited in manufacturing custom-tailored functional microstructures that are crucial to applications ranging from surface patterning to pharmaceutics.

Acknowledgement

The authors would like to thank Binita Pathak (Research Scholar at Indian Institute of Science) for her help in experiments, Pooja Sharma (Research Assistant at Indian Institute of Science) for acquiring SEM images and Dr. Debasis Sen (Bhabha Atomic Research Centre, BARC, India) for useful discussions during the course of this work.

References

1 N. Tsapis, D. Bennett, B. Jackson, , D.A. Weitz and D.A. Edwards, *Proc. Natl. Acad. Sci,.* 2002, 72, 12001.

2 K. Masters, *Spray Drying Handbook*, Fourth Edition, Halstead Press, New York, 1985.

3 L. Pauchard,Y. Couder, *EPL (Euro Phys. Lett.)*, 2004, 66(5), 667.

4 J. Bahadur, D. Sen, S. Mazumder, S. Bhattacharya, H. Frielinghaus and G. Goerigk, *Langmuir*, 2011, 27(13), 8404-8414.

5 J. Bahadur, D. Sen, S. Mazumder, B. Paul, H. Bhatt and S. G. Singh, *Langmuir*, 2012, 28(3), 1914-1923.

6 E. Katifori, S. Alben, E. Cerda, D.R. Nelson and J. Dumais, *Proc. Natl. Acad. Sci.* U.S.A., 2010, 107, 7635-7639.

7 Paulose, J., Nelson, D. R. Buckling pathways in spherical shells with soft spots. *Soft Matter*, *9*(34), 8227-8245 (2013).

8 S. S. Datta, S. H. Kim, J. Paulose, A. Abbaspourrad, D. R. Nelson and D. A. Weitz, *Physical review letters*, 2012, 109(13), 134302.

9 J. Paulose, G. Vliegenthart, G. Gompper, and D. R. Nelson, *Proc. Natl. Acad. Sci. U.S.A.,* 2012, 109, 19551.

10 D. Bushnell, *AIAA Journal*, 1981, 19(9), 1183-1226.

11 L. Pauchard and C. Allain, *Physical Review E*, 2003, 68(5), 052801.

12 L. Pauchard and C. Allain, *EPL (Euro Phys. Lett.)*, 2003, 62(6), 897.

13 Y. Gorand, L. Pauchard, G. Calligari, J. P. Hulin and C. Allain, *Langmuir*, 2004, 20(12), 5138-5140.

14 D. Sen, J. S. Melo, J. Bahadur, S. Mazumder, S. Bhattacharya, G. Ghosh, S. F. D'Souza, *The European Physical Journal E: Soft Matter and Biological Physics*, 2010, 31(4), 393-402.

15 A. Sanyal, S. Basu, S. Chowdhuri, , P. Kabi, S. Chaudhuri, *Applied Phys. Lett.*, 2014, 104(16), 163108.

16 D. Sen, J. S. Melo, J. Bahadur, S. Mazumder, S. Bhattacharya, S. F. D'Souza and R. Loidl, *Soft Matter*, 2011, 7(11), 5423-5429.

17 S. SacannaW. T. M. Irvine, P. M. Chaikin and D. J. Pine, *Nature*, 2010, 464(7288), 575-578.

18 J. Paulose, G. A. Vliegenthart, G. Gompper and D. R. Nelson, *Proc.Natl. Acad. Sci.*, 2012, 109(48), 19551-19556.

19 A. Fery and R. Weinkamer, *Polymer*, 2007, 48(25), 7221-7235.

20 E. Tijerino, S. Basu and R. Kumar, *Journal Appl. Phys.*, 2013, 113(3), 034307.

21 S. Basu, E. Tijerino and R. Kumar, *Appl. Phys. Lett.*, 2013, 102(14), 141602.

22 A. L. Yarin, G. Brenn, O. Kastner, and C. Tropea, *Phys. Fluid.,* 2002, 14(7), 2289-2298.

23 O. Kastner, G. Brenn, D. Rensink and C. Tropea, *Chem. Engg. Tech.,* 2001, 24(4), 335-339.

24 B. Park and R.L. Armstrong, *Appl. Opt.,* 1989, 28, 3671-3680.

25 A. L. Yarin, M. Pfaffenlehner and C. Tropea, *J. Fluid Mech.*, 1998, 356, 65-91.

26 A. L. Yarin, G. Brenn, O. Kastner, D. Rensink and C. Tropea, *J. Fluid Mech.*1999, 399, 151-204.

27 W. J. Xie and B. Wei, *Appl. Phys. Lett.*, 2007, 90(20), 204104-204104.

28 C. R. Wilke and P. Chang, *AIChE Journal*, 1955, 1(2), 264-270.

29 A. Saha, S. Basu, C. Suryanarayana and R. Kumar, *Int. J. Heat Mass Trans.*, 2010, 53(25), 5663-5674.

30 A. Saha, S. Basu and R. Kumar, *J. Fluid Mech.*, 2012, 692, 207-219.

31 A. Y. Rednikov, H. Zhao and S. S. Sadhal, E. H. Trinh, *The Quarterly J. Mech. Appl. Math.*, 2006, 59(3), 377-397.

32 V. Y Rudyak, A. A. Belkin and V. V. Egorov, *Technical Physics*, 2009, 54(8), 1102-1109.

33 N. Tsapis, E. R. Dufresne, S. S. Sinha, C. S. Riera, J. W. Hutchinson, L. Mahadevan and D. A. Weitz, *Phys. Rev. Lett.*, 2005, 94(1), 018302.

34 L. Landau and E. Lifshitz, *Theory of Elasticity*, Third Edition, Butterworth-Heinemann, 1986.

35 E. G. Lierke, *Acta Acustica United with Acustica*, 2002, 88(2), 206-217.

36 L. Pauchard, M. Mermet-Guyennet and F. Giorgiutti-Dauphiné, *Chem. Engg. Processing: Proc. Intens.*, 2011, 50(5), 483-485.

37 F. Boulogne, F. Giorgiutti-Dauphiné and L. Pauchard, *Soft Matter*, 2013, 9(3), 750-757.